

ALMA 873 μm Polarization Observations of the PDS 70 Disk

Hauyu Baobab Liu^{1,2,*}, Kiyoaki Doi^{3,4}, Simon Casassus^{5,6,7}, Akimasa Kataoka⁴, Ruobing Dong⁸, Jun Hashimoto⁹, and Philipp Weber^{10,11,12}

¹ Department of Physics, National Sun Yat-Sen University, No. 70, Lien-Hai Road, Kaohsiung City 80424, Taiwan, R.O.C.

² Center of Astronomy and Gravitation, National Taiwan Normal University, Taipei 116, Taiwan

³ Department of Astronomical Science, School of Physical Sciences, Graduate University for Advanced Studies (SOKENDAI), 2-21-1 Osawa, Mitaka, Tokyo 181-8588, Japan

⁴ National Astronomical Observatory of Japan, 2-21-1 Osawa, Mitaka, Tokyo 181-8588, Japan

⁵ Departamento de Astronomía, Universidad de Chile, Casilla 36-D, Santiago, Chile

⁶ Data Observatory Foundation, to Data Observatory Foundation, Eliodoro Yáñez 2990, Providencia, Santiago, Chile

⁷ Millennium Nucleus on Young Exoplanets and Their Moons (YEMS), Santiago, Chile

⁸ Kavli Institute for Astronomy and Astrophysics, Peking University, 5 Yiheyuan Road, Haidian District, Beijing, 100871, People's Republic of China

⁹ Institute of Astronomy and Astrophysics, Academia Sinica, 11F of Astronomy-Mathematics Building, AS/NTU No.1, Sec. 4, Roosevelt Rd, Taipei 10617, Taiwan, R.O.C.

¹⁰ Departamento de Física, Universidad de Santiago de Chile, Av. Víctor Jara 3493, Santiago, Chile

¹¹ Millennium Nucleus on Young Exoplanets and their Moons (YEMS), Chile

¹² Center for Interdisciplinary Research in Astrophysics Space Exploration (CIRAS), Universidad de Santiago, Chile

Received December 23, 2025

ABSTRACT

At a 112.4 pc distance, the PDS 70 protoplanetary disk is a rare case that has been confirmed to host two accreting planets. This makes it the most important laboratory for studying dust growth in the context of planet formation. Here we present the first deep, full polarization observations at 873 μm wavelength. We detected $\sim 1\%$ – 2.5% linear polarization over the bulk of the ~ 55 – 100 AU (sub)millimeter ring. The polarization position angles align preferentially with the projected minor axis of the disk. The standard interpretation is that the observed polarization is caused by dust self-scattering, with a maximum dust grain size of ~ 100 μm . On $\gtrsim 10$ AU scales, which can be resolved by the presented 873–3075 μm observations, the ring is marginally optical thick at 873 μm wavelength. Using Monte Carlo radiative transfer simulations, we found that an azimuthally asymmetric, marginally optically thick ring with a maximum dust grain size of ~ 87 μm can reproduce the observed 873 μm polarization position angles and percentages. This study indicates that the coagulation of ice-coated dust in the protoplanetary disk may be limited by fragmentation or bouncing.

Key words. Protoplanetary disks – Planets and satellites: formation – (ISM:) dust, extinction – Radio continuum: ISM

1. Introduction

For a region in the protoplanetary disk, formation of rocky planet is promoted if dust grains can grow to $\gtrsim 10^3$ μm sizes by coagulation. Once the dust grains reach this size, they can become partially dynamically decoupled from the surrounding gas and begin to drift toward pressure maxima (Weidenschilling 1977), which results in local dust overdensities. They can manifest as substructures in the protoplanetary disk. Inside these dust overdensities, various dynamical instabilities tend to make evolved dust spatially much more confined than gas. In the end, some of these dust concentrations may undergo self-gravitational contraction, resulting in the formation of kilometer-sized planetesimals (Birnstiel et al. 2016).

Why may grains grow to $\gtrsim 10^3$ μm in certain regions in a protoplanetary disk, but not necessarily everywhere? This is, to a large extent, because the stickiness of dust surface depends on the chemical composition, which depends on temperature. Inside the ~ 150 K isotherm, known as the water snowline, dust grains are primarily composed of astronomical silicate and carbonaceous material. In contrast, dust grains located outside the

water snowline are coated with significant amount of water ice. Most of the area in a protoplanetary disk is situated outside of the water snowline. Whether or not water-ice-coated dust grains are sticky enough to coagulate to $\gtrsim 10^3$ μm sizes efficiently, remain actively debated (Musiolik & Wurm 2019; Kimura et al. 2020). Moreover, planets that formed in low-temperature environments likely have high abundances of water and carbon. This poses challenges to reconciling with observations of our own Earth, where the carbon and water abundances are only about $\sim 0.1\%$ of those found in interstellar dust (Li et al. 2021).

To observationally test the capability of dust grains growing to millimeter sizes in regions with various grain compositions, we can examine the maximum dust grain size (a_{\max}) by probing the wavelength-dependent continuum spectral indices (α ; c.f. Appendix B for definition; Beckwith & Sargent 1991; Testi et al. 2014). This is because larger dust grains can emit more efficiently at longer wavelength. In theory, the most reliable constraint on a_{\max} can be given when the observations cover wavelengths that are comparable to and larger than a_{\max} . However, the values of a_{\max} inferred from such analyses often suffer from low precision and may be degenerate. Observationally, whether or not a_{\max} exceeds $\gtrsim 10^3$ μm on 10^0 – 10^2 AU scales has

* Corresponding author: hyliu.nsysu@g-mail.nsysu.edu.tw

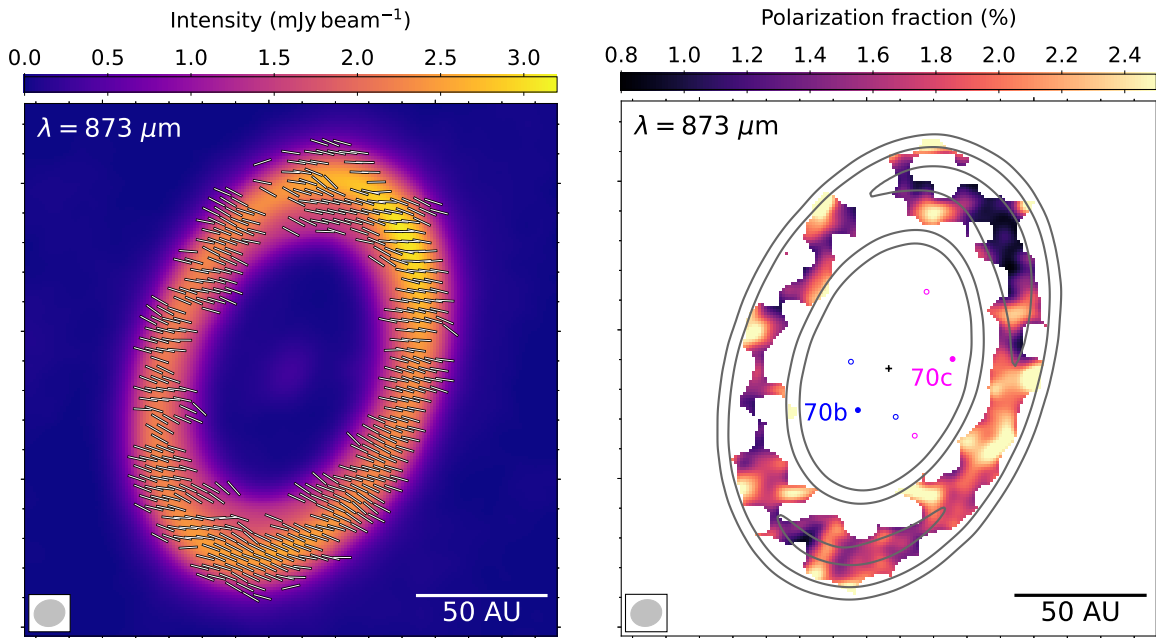


Fig. 1: The 873 μm full polarization images on PDS 70. Left panel shows the total intensity (color scale) and polarization position angles (line segments). Right panel shows the total intensity (contours) and the polarization fraction. Contour levels are 197 $\mu\text{Jy beam}^{-1}$ (5σ) $\times [3, 6, 12]$. The cross symbol marks the location of the host star. Filled and open circles mark the locations of PDS 70b and 70c, and their L4 and L5 points. Synthesized beam is shown in the lower left.

been a long-standing issue (Testi et al. 2014; Guidi et al. 2022; Sierra et al. 2025).

Investigation into the effects of dust self-scattering shed light on this problem. It was realized that the spectral index can be lowered in a narrow wavelength range close to $\lambda = 2\pi a_{\max}$ in which the dust albedo is high and is decreasing with wavelength. Confirming such lowering of spectral indices in multi-wavelength observations (e.g., based on fitting spectral energy distributions) therefore can precisely constrain a_{\max} to $\lesssim \lambda/2\pi$ (Liu 2019). For example, when dust emission is optically thick and falls within the Rayleigh-Jeans limit, resolving $\alpha \lesssim 2$ at 1200 μm wavelength implies $a_{\max} \lesssim 200 \mu\text{m}$.

In addition, self-scattered dust emission in an inclined dusty disk is linearly polarized (Kataoka et al. 2015). The polarization position angles preferentially align with the projected minor axis in an inclined disk, while they preferentially align in the radial directions in geometrically narrow, optically thin dusty rings (Kataoka et al. 2015; Pohl et al. 2016; Yang et al. 2016). Such features are most prominent when a_{\max} is close to the Mie region $a_{\max} \sim \lambda/2\pi$ (Kataoka et al. 2015; Yang et al. 2016). Theoretically, for spatially resolved observations at a given wavelength λ , the polarization percentage becomes much higher at the locations where a_{\max} is very close to $\lambda/2\pi$ (e.g., 1–3%; Kataoka et al. 2015). Comparing polarization observations with resolved total intensity spectral modeling is presently the most effective technique for accurately determining a_{\max} within the range of several tens of micrometers to centimeter sizes.

Direct near-infrared imaging observations have resolved two massive planets in the PDS 70 system ($d \sim 112.4$ pc; Gaia Collaboration et al. 2023), namely PDS 70b and 70c. The masses of these two planets were estimated to be $3.2^{+0.3}_{-1.6} M_{\text{Jup}}$ and $\lesssim 7.5\text{--}13.6 M_{\text{Jup}}$, respectively (Keppler et al. 2018; Haffert et al. 2019; Wang et al. 2021). The host star, PDS 70, is a K7-type ($0.85 M_{\odot}$; Keppler et al. 2019), ~ 5 Myr weak-line T Tauri type star (Keppler et al. 2018; Müller et al. 2018). The previ-

ous near-infrared imaging observations (Hashimoto et al. 2012; Keppler et al. 2018, 2019) resolved that PDS 70 is associated with an extended disk of ~ 100 AU radius, which presents a gap extending from $\sim 17\text{--}60$ AU radii. The high angular resolution (sub)millimeter imaging observations (Hashimoto et al. 2015; Isella et al. 2019; Keppler et al. 2019; Facchini et al. 2021; Casassus & Cárcamo 2022; Liu et al. 2024a; Doi et al. 2024; Sierra et al. 2025; Dominguez-Jamett et al. 2025) have resolved a $\sim 55\text{--}100$ AU dusty ring and an inner disk at < 17 AU radius. Constraining a_{\max} in this system provides the most direct indication for the natal environment of these two planets.

We performed full polarization observations toward PDS 70, at an angular resolution of $\lesssim 0''.1$, and at a wavelength of $\sim 873 \mu\text{m}$. These are the first (sub)millimeter polarization observations of a disk hosting protoplanets that have been confirmed by direct imaging. In addition, we performed the complementary, $\sim 0''.1$ resolution observations of total intensities (i.e., Stokes I) at ~ 2068 and $\sim 3075 \mu\text{m}$ wavelengths, and compared them with the publicly available observations at ~ 1226 and $1287 \mu\text{m}$ wavelengths at similar angular resolutions. We provide an outline of these observations in Section 2. The observational results are presented in Section 3. Our interpretation for the observational results and the physical implications are discussed in Section 4. The conclusion is given in Section 5. Appendix A provides the details of data calibration and imaging. Appendix B described how we measured spectral indices. While the present study has an emphasis on presenting the polarization observational results, nevertheless, we have produced a working model to compare with the observations using Monte Carlo radiative transfer simulations. We outline how the model was produced in Appendix C. More sophisticated modeling is beyond the scope of the present paper, which will be investigated in near future. Appendix D introduces how the dust fragmentation velocity (v_{frag}) can be estimated.

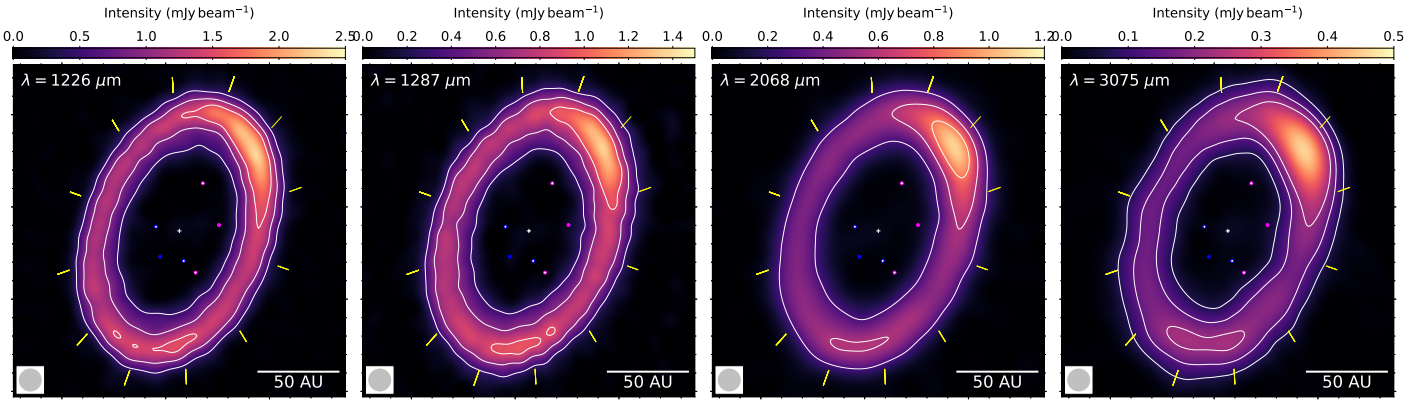


Fig. 2: Total intensity images at 1226, 1287, 2068, and 3075 μ m wavelengths. Contours for the $\lambda = 1226 \mu\text{m}$ image are $81 \mu\text{Jy beam}^{-1}$ (3σ) $\times [6, 12, 18]$; contours for the $\lambda = 1287 \mu\text{m}$ image are $60 \mu\text{Jy beam}^{-1}$ (3σ) $\times [5, 10, 15]$; contours for the $\lambda = 2068 \mu\text{m}$ image are $36 \mu\text{Jy beam}^{-1}$ (3σ) $\times [8, 16, 24]$; contours for the $\lambda = 3075 \mu\text{m}$ image are $18 \mu\text{Jy beam}^{-1}$ (3σ) $\times [4, 8, 12]$. Symbols are the same as those in Figure 1. Synthesized beams are shown in the lower left. Yellow line segments indicate the deprojected position angles starting from 0° (defined at the major axis in the northwest), with 30° intervals.

2. Data

2.1. New ALMA Observations

We resolved the (sub)millimeter dust continuum emission using the Atacama Large Millimeter/Submillimeter Array (ALMA). We carried out full polarization observations at Band 7, and carried out total intensity (Stokes I) observations at Bands 3 and 4. Basic information of these observations is summarized in Table 1. More technical details are given as follows.

2.1.1. Band 7 full polarization observations

There were 9 executions of high angular resolution observations, which were distributed on seven dates. Each execution has a ~ 3 hours' duration. There was 1 additional execution of short-spacing observations, which was in a relatively compact array configuration to recover the spatially extended emission. Concatenating all Band 7 observations yielded a $16\text{--}4002 k\lambda$ coverage of uv distances, which provides a maximum recoverable angular scale (MRS; estimated by $0.6\lambda/D$, where D is the shortest uv distance) of $3''.9$. This MRS is considerably larger than the projected major axis of the target source, PDS 70 (Hashimoto et al. 2015; Long et al. 2018). Therefore, our Band 7 observations are not subject to missing fluxes.

The correlator was configured to simultaneously provide full polarization products (XX, XY, YX, YY) in the four spectral windows that centered at 336.5, 338.5, 348.5, and 350.5 GHz frequencies. Each spectral window has a 1.875 GHz bandwidth, which was sampled by 1920 spectral channels. The mean wavelength of these observations was $873 \mu\text{m}$.

Besides our target source, PDS 70, the observations in each execution covered the absolute flux, passband, complex gain, and polarization calibrators. The calibrators for each epoch of observations were automatically selected by the observing script generator during the Phase 2 Group (P2G) stage.

2.1.2. Band 3 and Band 4 dual polarization observations

There were 2 executions of high angular resolution observations and 1 execution of short-spacing observations at Band 3 (Table 1). Concatenating all Band 3 observations yielded a $4.2\text{--}2979 k\lambda$ coverage of uv distances, which corresponds to an MRS of $14''.7$. There were 1 executions of high angular resolution obser-

vations and 1 execution of short-spacing observations at Band 3 (Table 1). Concatenating all Band 4 observations yielded a $6.5\text{--}3919 k\lambda$ coverage of uv distances, which corresponds to an MRS of $9''.5$.

For the Band 3 observations, the correlator was configured to provide dual polarization products (XX, YY) in the four spectral windows that centered at 90.5, 92.5, 102.5, 104.5 GHz; for the Band 4 observations, the correlator was configured to provide dual polarization products in the four spectral windows that centered at 138.0, 140.0, 150.0, 152.0 GHz. Each spectral window has a 1.875 GHz bandwidth, which was sampled by 3840 spectral channels. The mean wavelengths of these Band 3 and Band 4 observations were $3075 \mu\text{m}$ and $2068 \mu\text{m}$, respectively.

The observations in each execution of observations covered the target source PDS 70 and the absolute flux, passband, and complex gain calibrators, which can be looked up at the ALMA data archive¹.

2.2. Archival ALMA Band 6 observation

We retrieved the archival ALMA Band 6 observations, which were taken via project 2019.1.01619.S. There were two independent spectral tunings. Each spectral tuning employed one broad bandwidth (1.875 GHz) spectral window for observing continuum emission at high signal-to-noise ratios (SNR), and several narrow bandwidth spectral windows for observing spectral lines. We only utilized the data taken from the broad bandwidth spectral windows, which have centroid wavelengths of $1226 \mu\text{m}$ and $1287 \mu\text{m}$, respectively.

The observations at each tuning included short-spacing observations, which provided $\sim 0''.4$ angular resolutions, and high angular resolution observations, which provided $\sim 0''.1$ angular resolutions. Concatenating all $1226 \mu\text{m}$ observations yielded a $10.1\text{--}2674 k\lambda$ uv coverage, while concatenating all $1287 \mu\text{m}$ observations yielded a $9.8\text{--}2552 k\lambda$ uv coverage. The MRS of these observations are larger than those of our Band 7 observations (Table 1), which avoided missing fluxes. We refer to the previous publication of these observations (Facchini et al. 2021) for more technical details.

¹ <https://almascience.nrao.edu/aq/>

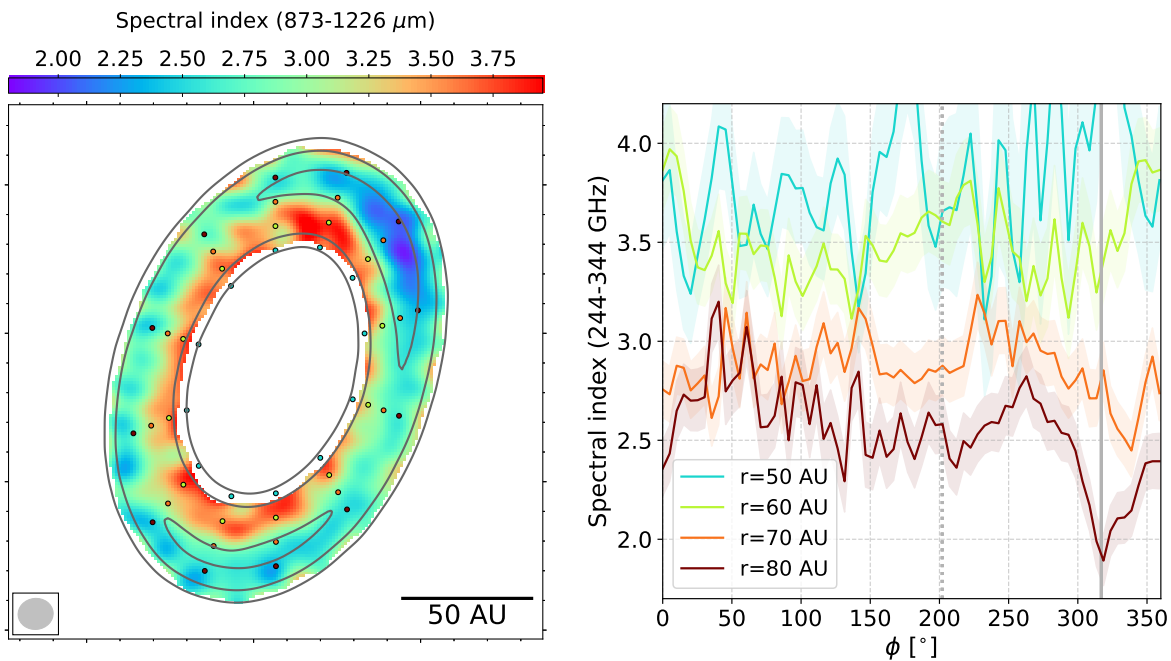


Fig. 3: The 873–1226 μm spectral index ($\alpha_{\text{b6-b7}}$). Color image in the left panel shows the spatially resolved distribution of $\alpha_{\text{b6-b7}}$. Contours are the same as those in the right panel of Figure 1. The circles (with 30° intervals in deprojected position angles) indicate the 50, 60, 70, and 80 AU deprojected radii. Right panel shows the values of $\alpha_{\text{b6-b7}}$ at 50, 60, 70, and 70 AU deprojected radii as functions of deprojected position angle ϕ .

3. Results

Figure 1 shows the Stokes I intensities, polarization position angles, and polarization fractions resolved at 873 μm wavelength. The Stokes I intensities at 1226, 1287, 2068, and 3075 μm wavelengths are presented in Figure 2, which have been smoothed to circular beams to allow diagnosing sub-structures without being confused by the smearing effect of asymmetric beams.

At these wavelengths, the total intensities trace an inclined ring and two crescents situated in the northwest and southwest of the PDS 70 ring (Figure 2). The higher intensity crescent in the northwest of the ring (hereafter the northwest-crescent) has been reported in the recent studies (Isella et al. 2019; Keppler et al. 2019; Liu et al. 2024a; Doi et al. 2024; Sierra et al. 2025; Dominguez-Jamett et al. 2025). The fainter one in the southwest (hereafter the southwest crescent) shows consistent angular offset from the projected major axis of the PDS 70 ring in the multi-wavelength observations (Figure 2). It is more evident in the images at 1226, 1287, 2068, and 3075 μm . The southwest crescent is less prominent at 873 μm and shorter wavelengths (Figure 1; Isella et al. 2019; Keppler et al. 2019; Sierra et al. 2025; Dominguez-Jamett et al. 2025) in spite of the better angular resolutions of these short wavelength observations, due to the high dust optical depths at short wavelengths (more below; Liu et al. 2024a; Sierra et al. 2025). Using Monte Carlo Radiative Transfer (MCRT) modeling (more below; c.f. Appendix C), we determined the deprojected centroid position angles (defined north-to-east with respect to the major axis) of northwest-crescent and southwest-crescent to be $317^\circ \pm 1^\circ$ and $225^\circ \pm 3^\circ$ respectively.

The morphology of the bulk of the PDS 70 ring can be described by a geometrically narrow belt (hereafter narrow-ring) centered at a radius of ~ 77 AU and superimposed on a fainter, radially more extended ring (hereafter wide-ring). The wide-ring has a larger extension inward of the 77 AU radius (Isella et al. 2019; Keppler et al. 2019; Doi et al. 2024).

We detected 873 μm linear polarization close to the radial range of the narrow-ring. The observations resolved azimuthal variations of the polarization fraction in the range of $\sim 1\%–2.5\%$. The polarization fraction is maximized in the west and presents a minimum at the northwest-crescent (Figure 1). The mean polarization position angles is 68° , which is close to that of the projected minor axis of the PDS 70 ring. The polarization position angles are rather uniform, with a modest observed dispersion of 27° . The actual dispersion of polarization position angles is smaller, considering that the observations are subject to thermal noise.

Figure 3 shows the spatially resolved spectral indices ($\alpha_{\text{b6-b7}}$) measured at 873–1226 μm wavelengths. In general, it is close to the interstellar value, 3.7, at the faint inner rim of the wide-ring, which is consistent with $a_{\text{max}} \lesssim 100 \mu\text{m}$ (Testi et al. 2014). The value of $\alpha_{\text{b6-b7}}$ is $\sim 2\text{--}3$ close to the narrow-ring (c.f. Fasano et al. 2025). In addition, $\alpha_{\text{b6-b7}}$ shows significant azimuthal variation in the narrow-ring. It has a minimum value of 1.86 ± 0.13 around the northwest crescent, indicating that dust emission at 873–1226 μm is likely very optically thick at this location.

4. Discussion

The observed 873 μm polarization and the $\alpha_{\text{b6-b7}}$ distributions can be concordantly explained if a_{max} in the bulk of the (sub)millimeter ring is $\lesssim 100 \mu\text{m}$. This is the first observational indication that the (sub)millimeter luminosity in a protoplanetary disk is dominated by $\lesssim 100 \mu\text{m}$ sized dust even after the formation of planets. The observed polarization position angles appear more like the case of an inclined disk rather than a ring for two reasons. First, the radial extension of the PDS 70 submillimeter ring is wide (e.g., compared to scale height, c.f. Table C.1). Second, at 873 μm wavelength, the ring is likely optically thick

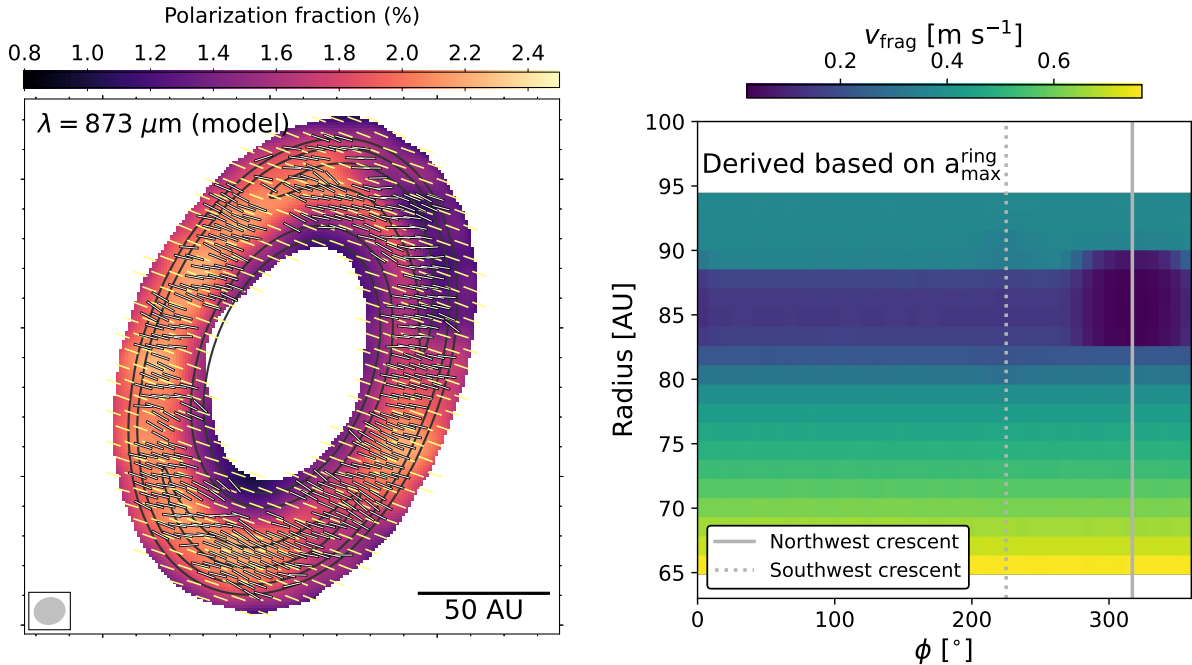


Fig. 4: Physical properties derived from the fiducial radiative transfer model. Left panel shows the synthesized, $\lambda = 873 \mu\text{m}$ images of total intensity (contours), polarization fraction (color), and polarization position angle (yellow line segments). We overplot the polarization position angles detected in actual observations (Figure 1). The angular resolution of these synthesized images are the same as those in Figure 1. Contour levels are $197 \mu\text{Jy beam}^{-1}$ (5σ) $\times [3, 6, 12]$. Synthesized beam is shown in the lower left. Right panel shows the fragmentation velocity (v_{frag}) derived based on the maximum dust grain sizes (a_{max}) in the PDS 70 rings.

in the azimuthal direction. These make the local radiative field around the narrow-ring effectively more like that in a disk.

To help understand the observational results, we constructed a model using Monte Carlo radiative transfer (MCRT) simulations and determined the free parameters in the model using the Markov Chain Monte Carlo (MCMC) method (see Appendix C). The main purpose of this model is to verify the qualitative interpretation of the observed $873 \mu\text{m}$ total intensity and polarization, rather than fitting the intensity distributions in detail. Figure 4 shows the synthesized $873 \mu\text{m}$ observations produced from our fiducial model. The total intensity distribution resembles the actual observations (Figure 1). It reproduces the azimuthally varying, $\sim 1\% \text{--} 2\%$ polarization produced due to dust self-scattering, with polarization position angles aligned with the minor axis of the (sub)millimeter ring.

In this model, the peak dust mass surface density is 0.4 g cm^{-2} in the narrow-ring, which are marginally optically thick at $\lesssim 1200 \mu\text{m}$ wavelengths. This results in $a_{\text{b6-b7}} \gtrsim 2$ in most of the narrow-ring. The maximum dust mass surface density is 0.093 g cm^{-2} in the wide-ring such that the (sub)millimeter ring becomes optically thin at its inner rim. The peak dust mass surface density in the northwest-crescent is 11 g cm^{-2} , which is optically thick at $\lesssim 1200 \mu\text{m}$ wavelengths. The values of a_{max} are $87 \mu\text{m}$ and $79 \mu\text{m}$ in the ring and in the northwest-crescent, respectively. The $873 \mu\text{m}$ polarization percentage is suppressed at the northwest-crescent primarily due to high optical depth rather than the spatial variation of a_{max} . The overall dust masses in the azimuthally symmetric rings, the northwest-crescent, and the southeast crescent are $103 M_{\oplus}$, $174 M_{\oplus}$, and $3.6 M_{\oplus}$, respectively. Our present model was based on the assumption of relatively compact dust grains (Appendix C.2.1, C.2.2, C.2.3). Considering a slight porosity (e.g. $\sim 80\%$ of volume is vacuum) may make the derived a_{max} values larger by a few times (Ueda et al. 2024),

which needs to be testified by future, multi-wavelength polarization observations and is beyond the scope of this paper.

The stickiness of dust can be characterized with the fragmentation velocity (v_{frag}), which is the largest relative velocity between two colliding dust particles that can still yield coagulation instead of fragmentation. Assuming that dust growth is limited by fragmentation rather than inward migration, which is realistic in the studies of dusty rings and crescent, v_{frag} can be inferred from the observed a_{max} values (Appendix D; Birnstiel et al. 2016). We found that v_{frag} in the bulk of the (sub)millimeter ring may be a fraction of 1 m s^{-1} (Figure 4). Even if we consider a realistic, small dust porosity (Ueda et al. 2024), v_{frag} (in m s^{-1} units) can only be as high as order of unity. Since the (sub)millimeter ring in PDS 70 is outside of the water snowline, the derived v_{frag} is in line with the recent laboratory experiments and theoretical studies which suggested water-ice-coated dust is not sticky (Musiolk & Wurm 2019; Kimura et al. 2020).

A caveat is that the present observations do not rule out the possibility that the observed $873 \mu\text{m}$ is partly contributed by emission of aligned dust (Hildebrand et al. 2000), which can be tested by future, multi-frequency full polarization ALMA observations.

5. Conclusion

We present the ALMA $873 \mu\text{m}$ full polarization observations and the complementary Stokes I observations at 1226 , 1287 , 2068 , and $3075 \mu\text{m}$ wavelengths, towards the planet-hosting dusty ring, PDS 70. The $873 \mu\text{m}$ observations detected $\sim 1\% \text{--} 2.5\%$ linear polarization. The polarization position angles are uniform, which approximately align with the projected minor axis of the PDS 70 dusty ring. Our observational results are consistent with a maximum dust grain size of $\lesssim 100 \mu\text{m}$. If this is indeed the case, then

Table 1: ALMA Observations

Start Time (UTC) (1)	End Time (UTC) (2)	b_{\min} (meters) (3)	b_{\max} (meters) (4)	uv Distance ($k\lambda$) (5)	Available Antennae (6)	PWV (mm) (7)
Band 7 (high-resolution)						
2023-05-23 00:23:41	2023-05-23 03:12:31	78	3637	79–3665	44	0.7–1.1
2023-06-01 22:14:09	2023-06-02 03:49:32	27	3637	64–3957	43	0.4–0.6
2023-06-03 22:39:50	2023-06-04 04:05:06	27	3637	29–3986	41	0.6–0.7
2023-06-07 22:51:33	2023-06-08 01:38:49	76	3637	82–4002	43	0.5–0.8
2023-06-08 23:22:52	2023-06-09 02:10:31	27	3637	79–3624	43	0.6–0.8
2023-11-27 10:32:06	2023-11-27 13:20:29	30	3697	26–3983	45	0.6–0.8
2023-11-28 10:40:07	2023-11-28 13:31:23	30	3637	27–3992	46	0.7–1.0
Band 7 (short-spacing)						
2023-01-23 09:23:26	2023-01-23 11:50:45	15	783	16–823	47	~0.4
Band 4 (high-resolution)						
2023-06-19 23:34:30	2023-06-20 00:45:48	91	8282	40–3319	44	1.8–2.1
Band 4 (short-spacing)						
2023-03-25 07:26:14	2023-03-25 07:41:46	15	1261	6.5–631	40	3.1–3.2
Band 3 (high-resolution)						
2023-07-02 21:54:49	2023-07-02 23:25:22	84	8547	25–2879	42	0.7–0.8
2023-07-02 23:46:31	2023-07-03 01:17:13	84	8547	24–2979	43	0.5–0.6
Band 3 (short-spacing)						
2023-03-26 04:56:48	2023-03-26 05:56:13	15	1397	4.2–432	46	4.7–5.4

Notes. Columns (1) and (2) are the start and end time of the scheduling block. Columns (3) and (4) are the shortest and longest baseline lengths. Column (5) is the range of projected baseline length. Column (6) is the number of available antennae during the observations. Column (7) is the range of precipitable water vapor during the observations.

our results imply that the fragmentation velocity of the water-ice-coated dust grains may be $\lesssim 1 \text{ m s}^{-1}$. Outside of water snowlines, the fragmentation and bouncing barriers may limit dust growth.

Acknowledgements. We deeply thank Dr. Conelis Duvelmond for the constructive comments. This paper makes use of the following ALMA data: ADS/JAO.ALMA#2019.1.01619.S and #2022.1.01477.S. ALMA is a partnership of ESO (representing its member states), NSF (USA) and NINS (Japan), together with NRC (Canada), MOST and ASIAA (Taiwan), and KASI (Republic of Korea), in cooperation with the Republic of Chile. The Joint ALMA Observatory is operated by ESO, AUI/NRAO and NAOJ. H.B.L. is supported by the National Science and Technology Council (NSTC) of Taiwan (Grant No. 113-2112-M-110-022-MY3). PW acknowledges support from the ANID – Millennium Science Initiative Program – Center Code NCN2024_001.

References

Beckwith, S. V. W. & Sargent, A. I. 1991, *ApJ*, 381, 250
 Bi, J., Lin, M.-K., & Dong, R. 2021, *ApJ*, 912, 107
 Birnstiel, T., Dullemond, C. P., Zhu, Z., et al. 2018, *ApJ*, 869, L45
 Birnstiel, T., Fang, M., & Johansen, A. 2016, *Space Sci. Rev.*, 205, 41
 CASA Team, Bean, B., Bhatnagar, S., et al. 2022, *PASP*, 134, 114501
 Casassus, S. & Cárcamo, M. 2022, *MNRAS*, 513, 5790
 Cazzoletti, P., van Dishoeck, E. F., Pinilla, P., et al. 2018, *A&A*, 619, A161
 Chung, C.-Y., Andrews, S. M., Gurwell, M. A., et al. 2024, *ApJS*, 273, 29
 Chung, C.-Y., Tsai, A.-L., Wright, M., et al. 2025, *ApJS*, 277, 45
 Delussu, L., Birnstiel, T., Miotello, A., et al. 2024, *A&A*, 688, A81
 Doi, K., Kataoka, A., Liu, H. B., et al. 2024, *ApJ*, 974, L25
 Dominguez-Jamett, O., Casassus, S., Liu, H. B., et al. 2025, arXiv e-prints, arXiv:2507.21970
 Dong, R., Hashimoto, J., Rafikov, R., et al. 2012, *ApJ*, 760, 111
 Dong, R., Liu, S.-Y., & Fung, J. 2019, *ApJ*, 870, 72
 Dullemond, C. P., Juhasz, A., Pohl, A., et al. 2012, RADMC-3D: A multi-purpose radiative transfer tool, *Astrophysics Source Code Library*, record ascl:1202.015
 Facchini, S., Teague, R., Bae, J., et al. 2021, *AJ*, 162, 99
 Fasano, D., Benisty, M., Curone, P., et al. 2025, *A&A*, 699, A373
 Gaia Collaboration, Vallenari, A., Brown, A. G. A., et al. 2023, *A&A*, 674, A1
 Garufi, A., Carrasco-González, C., Macías, E., et al. 2025, *A&A*, 694, A290
 Guidi, G., Isella, A., Testi, L., et al. 2022, *A&A*, 664, A137
 Haffert, S. Y., Bohn, A. J., de Boer, J., et al. 2019, *Nature Astronomy*, 3, 749
 Hartmann, L., Calvet, N., Gullbring, E., & D'Alessio, P. 1998, *ApJ*, 495, 385
 Hashimoto, J., Dong, R., Kudo, T., et al. 2012, *ApJ*, 758, L19
 Hashimoto, J., Tsukagoshi, T., Brown, J. M., et al. 2015, *ApJ*, 799, 43
 Hildebrand, R. H., Davidson, J. A., Dotson, J. L., et al. 2000, *PASP*, 112, 1215
 Hoang, T., Lan, N.-Q., Vinh, N.-A., & Kim, Y.-J. 2018, *ApJ*, 862, 116
 Isella, A., Benisty, M., Teague, R., et al. 2019, *ApJ*, 879, L25
 Kataoka, A., Muto, T., Momose, M., et al. 2015, *ApJ*, 809, 78
 Kataoka, A., Okuzumi, S., Tanaka, H., & Nomura, H. 2014, *A&A*, 568, A42
 Keppler, M., Benisty, M., Müller, A., et al. 2018, *A&A*, 617, A44
 Keppler, M., Teague, R., Bae, J., et al. 2019, *A&A*, 625, A118
 Kimura, H., Wada, K., Kobayashi, H., et al. 2020, *MNRAS*, 498, 1801
 Laor, A. & Draine, B. T. 1993, *ApJ*, 402, 441
 Li, J., Bergin, E. A., Blake, G. A., Ciesla, F. J., & Hirschmann, M. M. 2021, *Science Advances*, 7, eabd3632
 Li, J. I.-H., Liu, H. B., Hasegawa, Y., & Hirano, N. 2017, *ApJ*, 840, 72
 Liu, H. B. 2019, *ApJ*, 877, L22
 Liu, H. B., Casassus, S., Dong, R., et al. 2024a, *ApJ*, 972, 163
 Liu, H. B., Mérard, A., Green, J. D., et al. 2019, *ApJ*, 884, 97
 Liu, H. B., Muto, T., Konishi, M., et al. 2024b, *A&A*, 685, A18
 Liu, Y., Li, D., Wang, H., et al. 2025, *Science China Physics, Mechanics, and Astronomy*, 68, 259511
 Liu, Y., Linz, H., Fang, M., et al. 2022, *A&A*, 668, A175
 Long, Z. C., Akiyama, E., Sitko, M., et al. 2018, *ApJ*, 858, 112
 Lynden-Bell, D. & Pringle, J. E. 1974, *MNRAS*, 168, 603
 Müller, A., Keppler, M., Henning, T., et al. 2018, *A&A*, 617, L2
 Musiolik, G. & Wurm, G. 2019, *ApJ*, 873, 58
 Ohashi, S., Kataoka, A., van der Marel, N., et al. 2020, *ApJ*, 900, 81
 Painter, C., Andrews, S. M., Chandler, C. J., et al. 2025, *The Open Journal of Astrophysics*, 8, 134
 Pinilla, P., Benisty, M., Waters, R., Bae, J., & Facchini, S. 2024, *A&A*, 686, A135
 Pohl, A., Kataoka, A., Pinilla, P., et al. 2016, *A&A*, 593, A12
 Pollack, J. B., Hollenbach, D., Beckwith, S., et al. 1994, *ApJ*, 421, 615
 Rau, U. & Cornwell, T. J. 2011, *A&A*, 532, A71
 Sault, R. J., Hamaker, J. P., & Bregman, J. D. 1996, *A&AS*, 117, 149
 Sault, R. J., Teuben, P. J., & Wright, M. C. H. 1995, in *Astronomical Society of the Pacific Conference Series*, Vol. 77, *Astronomical Data Analysis Software and Systems IV*, ed. R. A. Shaw, H. E. Payne, & J. J. E. Hayes, 433
 Sierra, A., Benisty, M., Pinilla, P., et al. 2025, *MNRAS*, 541, 3101
 Stephens, I. W., Lin, Z.-Y. D., Fernández-López, M., et al. 2023, *Nature*, 623, 705
 Tazaki, R. & Tanaka, H. 2018, *ApJ*, 860, 79
 Tazaki, R., Tanaka, H., Kataoka, A., Okuzumi, S., & Muto, T. 2019, *ApJ*, 885, 52
 Testi, L., Birnstiel, T., Ricci, L., et al. 2014, in *Protostars and Planets VI*, ed. H. Beuther, R. S. Klessen, C. P. Dullemond, & T. Henning, 339–361

Ueda, T., Tazaki, R., Okuzumi, S., Flock, M., & Sudarshan, P. 2024, *Nature Astronomy*, 8, 1148

Vaillancourt, J. E. 2006, *PASP*, 118, 1340

van der Marel, N., van Dishoeck, E. F., Bruderer, S., et al. 2013, *Science*, 340, 1199

Wang, J. J., Vigan, A., Lacour, S., et al. 2021, *AJ*, 161, 148

Weidenschilling, S. J. 1977, *MNRAS*, 180, 57

Yang, H. & Li, Z.-Y. 2020, *ApJ*, 889, 15

Yang, H., Li, Z.-Y., Looney, L., & Stephens, I. 2016, *MNRAS*, 456, 2794

Yang, H., Stephens, I. W., Lin, Z.-Y. D., et al. 2025, *ApJ*, 989, L43

Yoshida, T. C., Curone, P., Stadler, J., et al. 2025, *ApJ*, 984, L19

Appendix A: ALMA Data Reductions

A.1. ALMA Data Calibration

For the observations introduced in Section 2, we downloaded the raw data and followed the standard procedure to perform data calibration using the CASA software package (CASA Team et al. 2022). Afterwards, we used the CASA tasks `phaseshift` and `fixplanets` to correct the central position of PDS 70 in all epochs of observations to that on UTC 2023 June 01, assuming that the proper motion (Gaia Collaboration et al. 2023) is $-29.697 \text{ mas yr}^{-1}$ in R.A. and is $-24.041 \text{ mas yr}^{-1}$ in Decl., respectively.

For each epoch of observations, we derived the gain-phase self-calibration solutions using aggregated continuum bandwidths and then applied the solutions to individual spectral windows. The gain-phase self-calibrations for the high angular resolution Band 3 observations (Table 1) and the high angular resolution Band 6 observations at $1287 \mu\text{m}$ wavelength failed due to the limited SNR. Nevertheless, the weather was very good during our observations. We visually inspected the data during the standard data calibration processes and found that the phase noises are not very large after flagging some bad scans. Therefore, we do not expect significant losses of intensity due to decoherence.

A.2. Imaging of ALMA Observations

Using the CASA software package, we performed multi-frequency synthesis (`mfs`) imaging (Rau & Cornwell 2011) using 1 Taylor coefficient in the spectral model (i.e., `nterms`=1). Due to a realistic consideration of computing power, before performing imaging, we binned the data such that the channel widths are $\lesssim 60 \text{ MHz}$. In this case, within the radius of the PDS 70 disk, frequency smearing leads to much lower than 1% loss of flux densities at all frequency bands we utilized. We created all images using $0''.01$ pixel sizes. We performed primary beam correction for all images.

A.2.1. Band 7 polarization images

We imaged the polarization-calibrated Band 7 data, which were not gain-phase self-calibrated. In this way, the Stokes I imaging process was limited by the intensity dynamic ranges owing to the residual phase errors. As a consequence, the Stokes I image is noisier than the Stokes Q and U images. This decision stems from the fact that the target source, PDS 70, exhibits spatially resolved, linearly polarized intensities. If we were to use the Stokes I image for gain-phase self-calibration of the XX and YY observations, it would disrupt the polarization properties of the target source (Sault et al. 1996). The effects include artificially suppressing the polarization percentage and rotating the polarization position angles. In principle, self-calibrating the full polarization data rather than dual polarization data can avoid this effect. However, the signal-to-noise ratios (SNRs) observed in the XY and YX polarizations were not high enough to support full-polarization gain-phase self-calibration.

We tried Briggs Robust=0 and Robust=2 weighting and found that only the latter provided high enough SNR for robustly detecting dust polarization. The Robust=2 weighted Stokes I , Q , and U images achieved the synthesized beam of $0''.105 \times 0''.089$ (P.A.= -76°) and the rms noises of 39, 7.6, and $7.5 \mu\text{Jy beam}^{-1}$, respectively.

We prepared the polarization intensity, polarization position angle, and polarization percentage images using the CARMA version of MIRIAD software package (Sault et al. 1995). Polarization percentages and polarization position angles were derived in the regions where the polarization and Stokes I intensities were detected at $>3\sigma$ and 15σ , respectively. The polarization intensities (PI) (and the subsequently derived polarization percentages) have been de-biased (i.e., $PI = \sqrt{Q^2 + U^2 - \sigma^2}$, where σ is the thermal noise; Vaillancourt 2006). The Stokes I , polarization intensity, polarization percentage, and polarization position angle images prepared this way are shown in Figure 1.

A.2.2. Stokes I images

We have tried various imaging parameters (e.g., Robust parameters, uv range, etc). In the following, we only introduced those that were directly used in the analyses presented in this paper.

1. We imaged the gain-phase self-calibrated Band 7 data using Robust=0 weighting and full uv distance range, to produce the high angular resolution, high fidelity $873 \mu\text{m}$ Stokes I image. This image provides good constraints on the widths of the structures in our MCMC fitting. The achieved synthesized beam and rms noises are $0''.064 \times 0''.056$ (P.A.= -49°) and $12 \mu\text{Jy beam}^{-1}$, respectively.
2. Without limiting the uv distance ranges, we imaged the gain-phase self-calibrated Band 3 ($3075 \mu\text{m}$) and Band 4 ($2068 \mu\text{m}$) data using Robust=2 weighting, and imaged the calibrated Band 6 $1287 \mu\text{m}$ data and the gain-phase self-calibrated Band 6 $1226 \mu\text{m}$ data using Robust=0 weighting. The achieved synthesized beam sizes and rms noises for these $3075 \mu\text{m}$, $2068 \mu\text{m}$, $1287 \mu\text{m}$, and $1226 \mu\text{m}$ images are $(0''.210 \times 0''.145; \text{P.A.}=-55.6^\circ; 5.9 \mu\text{Jy beam}^{-1})$, $(0''.180 \times 0''.164; \text{P.A.}=-58.8^\circ; 12 \mu\text{Jy beam}^{-1})$, $(0''.104 \times 0''.0797; \text{P.A.}=-84.4^\circ; 22 \mu\text{Jy beam}^{-1})$, $(0''.118 \times 0''.104; \text{P.A.}=-84.2^\circ; 28 \mu\text{Jy beam}^{-1})$, respectively. These images, with elliptical synthesized beams, were directly used in our MCMC fittings (see below). For the purpose of diagnosing azimuthally asymmetric substructures, we further smoothed these images to the circular synthesized beams, of which the full width at half maxima (FWHM) are the same as the FWHM of the major axes of the elliptical beams (Figure 2).
3. For the purpose of deriving spectral indices (Figure 3), we produced images by limiting the uv distance ranges to $16\text{--}2600 k\lambda$. We imaged the gain-phase self-calibrated Band 7 data using Robust=2 weighting, and imaged the gain-phase self-calibrated Band 6, $1226 \mu\text{m}$ data using Robust=0 weighting. The former and latter achieved the synthesized beams and rms noise of $(0''.111 \times 0''.097; \text{P.A.}=-63.7^\circ; 12 \mu\text{Jy beam}^{-1})$ and $(0''.118 \times 0''.104; \text{P.A.}=-84.2^\circ; 28 \mu\text{Jy beam}^{-1})$, respectively. We smoothed both images to the common, $0''.118 \times 0''.104$ (P.A.= -84.2°) synthesized beam before measuring spectral indices.

We note that since the high angular resolution Band 6, 1287 μ m data cannot be self-calibrated. Therefore, the Band 6, 1287 μ m data are not ideal for the purpose of deriving spatially resolved spectral indices. In particular, decoherence of signal and smearing of structures due to the residual phase errors can lead to underestimates of intensities at 1287 μ m. Nevertheless, while the residual phase errors have a more serious impact on the long-baseline data, the measurements of spatially integrated flux densities rely more on the short-spacing observations, which were gain-phase self-calibrated. Therefore, the integrated flux densities measured at 1287 μ m are reliable.

Appendix B: Spectral indices

We derived spectral indices (α) based on

$$\log\left(\frac{F_1}{F_2}\right) = \alpha \log\left(\frac{\nu_1}{\nu_2}\right), \quad (\text{B.1})$$

where F_1 and F_2 are the flux densities observed at frequency ν_1 and ν_2 , respectively. Uncertainties of α were derived considering standard error propagation, while the error (σ) incorporates the thermal noise σ_{th} (i.e., the root-mean-square of the intensities measured in the images) and absolute flux calibration error σ_{abs} as $\sigma = \sqrt{\sigma_{\text{th}}^2 + \sigma_{\text{abs}}^2}$. For each epoch of observations, we assumed that the absolute flux calibration error is a Gaussian random variable. We quoted the nominal 1- σ absolute flux calibration error (per execution of observation), $\sigma_{\text{abs}}^{\text{exc}}$, from the ALMA Cycle 11 Technical Handbook². We adopted $\sigma_{\text{abs}} = \sigma_{\text{abs}}^{\text{exc}} / \sqrt{N^{\text{exc}}}$, where N^{exc} is the number of executions of observations that have comparable or better than 0''.1 angular resolutions (c.f. Table 1 and the earlier observational study; Facchini et al. 2021).

Our approach slightly overestimated σ , thereby overestimating the uncertainties of α due to the following two reasons. First, the $\sigma_{\text{abs}}^{\text{exc}}$ is a constant for each epoch of observation, while our formulation treated it as an independent random variable at each independent spatial resolution unit (i.e., Gaussian beam width). Second, while N^{exc} only considered the high angular resolution executions of ALMA observations, the short-spacing executions, in fact, can also contribute to noise cancelling. The uncertainties of $\alpha_{\text{b6-b7}}$ presented in the right panel of Figure 3 should be regarded as conservative upper limits. The actual uncertainties of $\alpha_{\text{b6-b7}}$ should be smaller, although it is hard to quantify exactly how much smaller it is.

Appendix C: Radiative Transfer Model

Aiming at addressing the properties of dust that dominates the total intensities and polarization at 873 μ m wavelength, based on MCRT simulations, we constructed a model to compare with the observations on PDS 70. This approach is advantageous for our present purpose, since dust scattering is a non-local radiative transfer problem. Limited by the high computing cost of MCRT simulations, presently, our models for dust density distributions (see below) involve simplifications which help reduce the number of free parameters. In addition, we avoided including high-density compact (e.g., sub-AU scales) sub-structures which cannot be accurately modeled in the MCRT simulations without using a prohibitively large number of photons. Owing to these reasons, we do not attempt to reproduce the detailed intensity distributions at all wavelengths (more in the Caveats and limitations subsection). Therefore, our fiducial model does not falsify the possibilities of embedding some grown (e.g., $a_{\text{max}} > 1000 \mu\text{m}$) dust in the mid-plane of the PDS 70 disk (Liu et al. 2024a; Sierra et al. 2025). The current results show that this approach is promising. Future improvements could arise when increased computing power allows for more flexibility in the assumptions regarding dust density distributions.

Similar to the previous studies (Hashimoto et al. 2012; Dong et al. 2012; Hashimoto et al. 2015), our model includes a smooth disk that has sub- μ m dust sizes (hereafter small-dust disk; Appendix C.2.1), and other dusty structures (i.e., rings and crescents; Appendix C.2.2, C.2.3) that the a_{max} values are $\gg 1 \mu\text{m}$. Incorporating the small-dust disk is essential for accurately reproducing the optical and infrared SEDs. This contributes to building a realistic three-dimensional thermal profile, which is useful for examining the effects of dust self-scattering. Including the $a_{\text{max}} \gg 1 \mu\text{m}$ dusty structures is necessary for reproducing the (sub)millimeter intensity distributions resolved in the ALMA observations.

We note that the previous studies, which were based on lower angular resolution observations, approximated the (sub)millimeter ring using power-law radial density profiles (Hashimoto et al. 2012; Dong et al. 2012; Hashimoto et al. 2015; Long et al. 2018; Keppler et al. 2019). In our present study, motivated by high angular resolution images (Figure 1, 2; Keppler et al. 2019; Doi et al. 2024), we approximated the (sub)millimeter ring using a combination of a truncated narrow Gaussian ring and a truncated wide Gaussian ring. In addition, we superimposed two dust crescents (crescent-NW, crescent-SW) located in the northwest and southwest of the (sub)millimeter ring, respectively. The details of these components on our model will be introduced in the following subsections.

We based on the following steps to construct the radiative transfer model:

1. Using MCRT simulations, we interactively varied the free parameters of the two rings (wide and narrow) and the two crescents (northwest and southwest) until the synthesized (sub)millimeter SED approximate the observed one. Then, we optimize the free parameters of the small-dust disk for reproducing the optical and infrared SED summarized the previous work (Hashimoto et al. 2012), based on the MCRT simulations and MCMC method. The approach is plausible since the PDS 70 disk is optically thick at infrared and shorter wavelengths. In this case, small variations of the models for the rings and crescents do not significantly affect the synthesized optical and infrared SED. Conversely, due to the small dust sizes, the small-dust disk makes negligible contribution to the (sub)millimeter intensities. We verified these statements using the MCRT simulations.

² <https://almascience.nrao.edu/proposing/technical-handbook>

2. We fixed the free parameters of the small-dust disk, and based on the MCRT simulations and MCMC method to optimize the free parameters for the narrow- and wide-rings for reproducing the intensity distributions resolved over the position angle range 35° – 125° in the ALMA 873, 1226, 1287, 2068, and 3075 μm observations. We selected this position angle range since in our visual inspection the two crescents do not extend into it.
3. We fixed the free parameters of the small-dust disk and the narrow- and wide-ring, and based on the MCRT simulations and MCMC method to optimize the free parameters for the northwest and southwest crescents. The optimizations were for reproducing the observed intensity distributions over the position angle ranges of 220° – 60° and 130° – 215° , respectively.

When optimizing the parameters for the small-dust disk in Step 1, the log likelihood was derived based on the comparison with the previously published 0.365–90 μm data (Hashimoto et al. 2012):

$$\ln p(F|R_c, \beta, h_{100}) = -\frac{1}{2} \sum_n \left(\frac{F_n^{\text{data}} - F_n^{\text{model}}}{\delta F_n} \right)^2, \quad (\text{C.1})$$

where F_n^{data} and δF_n are the observed flux density and error of flux density of the n^{th} measurement, and F_n^{model} is the flux density of the RADMC-3D model at the wavelength of that measurement.

In Steps 2 and 3, the log likelihood was defined as

$$\ln p(F|\text{parms}) = -\frac{1}{2} \sum_{n,i} \left(\frac{I_{n,i}^{\text{data}} - I_{n,i}^{\text{model}}}{\delta I_{n,i}} \right)^2, \quad (\text{C.2})$$

where parms denote the free parameters mentioned above, $I_{n,i}^{\text{data}}$ and $\delta I_{n,i}$ are the observed intensity and error of intensity of the i^{th} pixel of the n^{th} image we compared with, and $I_{n,i}^{\text{model}}$ is the intensity of the RADMC-3D model at that pixel and wavelength of the n^{th} image we compared with. We evaluated $\ln p(F|\text{parms})$ from the regions where the intensities (polarization intensity) were detected at $>5\sigma$ ($>3\sigma$), to avoid fitting the low-brightness artifacts that can be produced in the interferometric imaging processes and to avoid the positive biases in the polarization intensities (Vaillancourt 2006). We note that although the Stokes Q and U images are not positively biased as the polarization intensity image, when the SNR are limited, it is hard to distinguish real negative Stokes Q and U intensities from thermal noises and interferometric imaging artifacts. Therefore, directly comparing the MCRT model with the observed Stokes Q and U intensities still requires truncating the regions that are below 3σ significance. In this case, when the polarization position angles are uniform, comparing the Stokes Q and U intensities separately and comparing with the polarization intensity are not fundamentally different. Finally, we masked the inner 0''25 projected radius to avoid being confused by the inner disk.

We selected to compare our MCRT model with the following observational images (Appendix A)

1. The Robust=2 weighted 873 μm polarization intensity image
2. The Robust=0 weighted 873 μm Stokes I intensity image
3. The Robust=0 weighted 1226 μm Stokes I intensity image
4. The Robust=0 weighted 1287 μm Stokes I intensity image
5. The Robust=2 weighted 2068 μm Stokes I intensity image
6. The Robust=2 weighted 3075 μm Stokes I intensity image

out of the consideration of optimizing the angular resolution versus SNR.

The computational cost of our approach is high, although it is still manageable. The MCMC walkers in all three steps converged in approximately 200 iterations. We chose the parameters of our fiducial model to be the 50th percentiles of the MCMC samplers after discarding the burnt-in steps. The fiducial model successfully reproduced the most prominent features resolved in the ALMA observations. The results of our fitting are summarized in Table C.1. Except for $\Sigma_0^{\text{narrow-ring}}$, the best-fit parameters and the uncertainties were defined by the 16th, 50th, and 84th percentiles of the MCMC samplers. We remark that the best-fit $a_{\text{max}}^{\text{crescent-NW}}$ value is very close to the best-fit value of $a_{\text{max}}^{\text{ring}}$ in spite of the very different intensities and 873 μm polarization percentages observed in the ring and in the crescent-NW (Figure 1).

Figure C.1 compares the SED produced from our fiducial model with the observed SEDs. There is a good consistency between the observed and synthesized SEDs at $<3000 \mu\text{m}$ wavelength (i.e., $>100 \text{ GHz}$). Compared to the observations, the synthesized SED of our model shows excess at $>3000 \mu\text{m}$ wavelength. We attribute it to the emission mechanisms that we did not consider in the present model (e.g., free-free emission, or the thermal emission of spinning nanometer-sized dust) and the localized high-density dust concentrations that may have $a_{\text{max}} \sim 1 \text{ mm}$, which were discussed in the previous work (Liu et al. 2024a). The free-free emission or the thermal emission of spinning nanometer-sized dust are likely very faint at the wavelength coverages of our ALMA observations (Hoang et al. 2018; Chung et al. 2025; Garufi et al. 2025; Painter et al. 2025), which should not confuse our modeling (Liu et al. 2024a). The localized high-density dust concentrations are likely situated in the disk mid-plane. If the localized high-density dust concentrations are in the northwest dust crescent, they should be obscured at 873 μm wavelengths. Without considering them will not make an impact on our modelings for the ALMA Band 7 (873 μm) polarization observations. However, since the localized high-density dust concentrations can contribute to significant flux densities at long wavelength bands (e.g., 2068–3075 μm), in terms of SED fittings, ignoring the localized high-density dust concentrations tend to make us slightly overestimate the dust column densities and a_{max} in the rings and crescents.

We remark that, ideally, it is more accurate if we optimize the free parameters of all components (i.e., small-dust, narrow-/wide-rings, crescent-NW/SW) in the model simultaneously. However, with this approach, considering the realistic computing power, the parameter space is significantly larger than what can be feasibly explored by the MCMC samplers. Yet the improved accuracy will only yield improvement on some subtle details that are minor to our present science purpose.

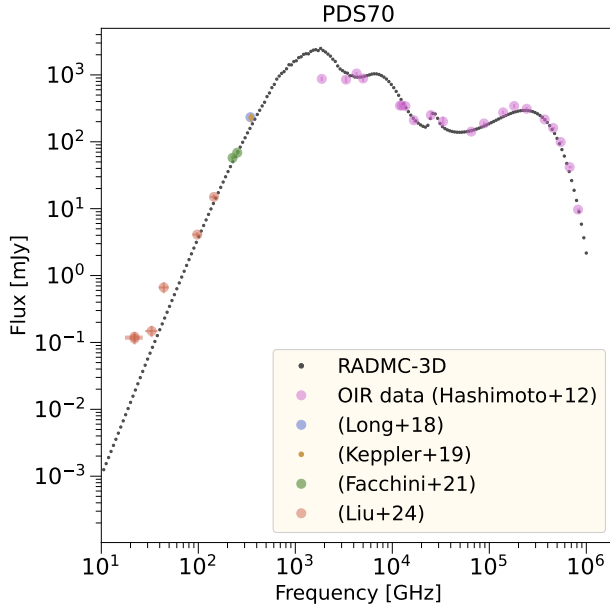


Fig. C.1: A comparison between the fiducial SED model (black dots; Methods) and observational data (colorful dots; Hashimoto et al. 2012; Long et al. 2018; Keppler et al. 2019; Facchini et al. 2021; Liu et al. 2024a).

C.1. Evaluating dust opacity

We evaluated wavelength-dependent dust opacities (including full scattering matrices) using the publicly available `optool` package³. We assumed that the size distributions of dust follow $n(a) \propto a^p$ between the minimum and maximum dust grain sizes, a_{\min} and a_{\max} . Since our main purpose is to model the emission of grown dust that is trapped in the PDS 70 ring, we assumed $p = -3.5$, which is consistent with fragmentation limited dust growth instead of inward-drift limited dust growth (Birnstiel et al. 2016). In general, the $p = -3.5$ assumption provides upper limits of a_{\max} . If we make p larger (e.g., $p = -3$ or $p = -2.5$; Sierra et al. 2025), a larger fraction of overall dust mass will be in the form of grown dust, which in turn leads to a smaller a_{\max} value in the fiducial SED model.

C.2. Density distribution

We assumed that the PDS 70 disk is 51.7° inclined and has a 160.1° position angle (Keppler et al. 2019). We have checked that these parameters can approximate the (sub)millimeter Stokes I intensity distributions presented in this work (Figure 1, 2).

C.2.1. Small-dust disk

Since small dust grains are well coupled with gas, we followed the previous works (Dong et al. 2012; Hashimoto et al. 2015) to parametrize the (vertically integrated) dust mass surface density ($\Sigma^{\text{small-dust}}(R)$) outside the gap radius (R_{gap}) in cylindrical-polar coordinates $\{R, z\}$ using a modified formulation for viscous accretion gaseous disk (Lynden-Bell & Pringle 1974; Hartmann et al. 1998):

$$\Sigma^{\text{small-dust}}(R) = \Sigma_0^{\text{small-dust}} \left(\frac{R}{R_c} \right)^{-q} \exp \left[- \left(\frac{R}{R_c} \right)^{2-q} \right], \quad (\text{C.3})$$

where R_c is the characteristic radius of the small-dust disk. Inside R_{gap} , we assumed that $\Sigma^{\text{small-dust}}(R)$ is δ_{cav} times smaller than what is described by Equation C.3, where δ_{cav} is a constant depletion factor. To reduce the number of free parameters, we assumed $q = 1$ following the previous works (Hashimoto et al. 2012; Dong et al. 2012; Hashimoto et al. 2015). We adopted $R_{\text{gap}} = 54$ AU according to the previous observations (Keppler et al. 2018). Figure C.2 shows the resulting $\Sigma^{\text{small-dust}}(R)$.

We evaluated the dust mass volume density distribution $\rho(R, z)$ by

$$\rho(R, z) = \frac{\Sigma^{\text{dust}}(R)}{\sqrt{2\pi} h(R)} \exp \left[-\frac{1}{2} \left(\frac{z}{h(R)} \right)^2 \right], \quad (\text{C.4})$$

where $h(R)$ is the characteristic scale height (see below) at radius R , and $\Sigma^{\text{dust}}(R) = \Sigma^{\text{small-dust}}(R)$ for the model of the small-dust disk. Following the previous works (Hashimoto et al. 2012; Dong et al. 2012; Hashimoto et al. 2015), for the small-dust disk, we

³ <https://github.com/cdominik/optool>

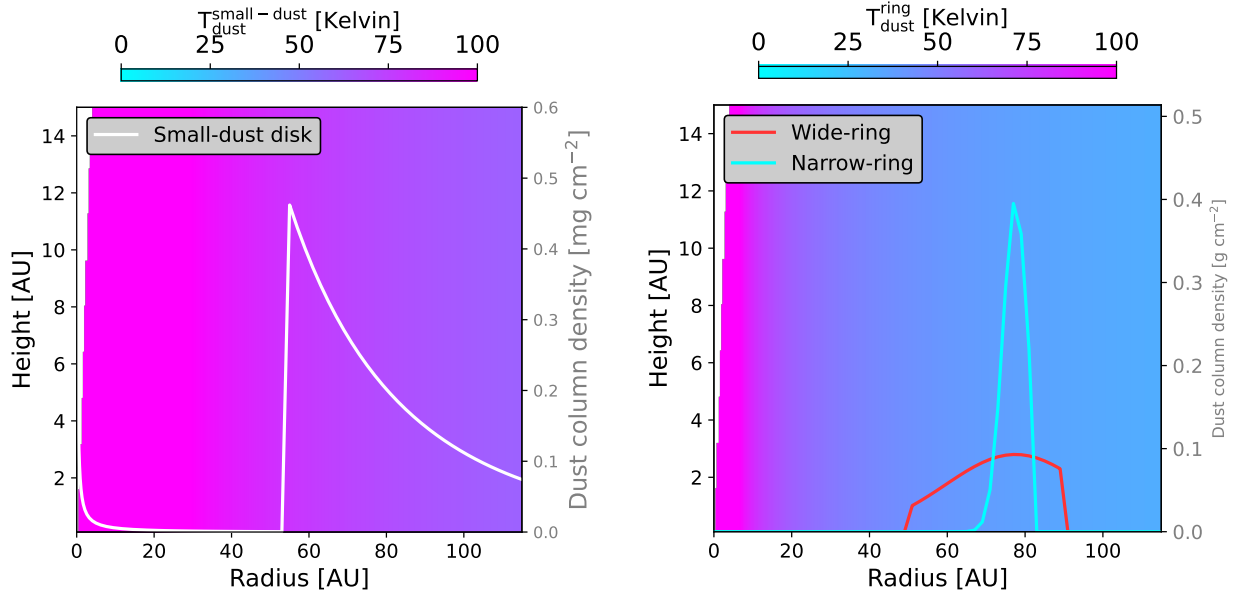


Fig. C.2: Temperature (color) and dust column density (solid lines) profiles of the fiducial model (Methods). Left and right panels show these properties of the small-dust disk and the dust rings, respectively. Both panels present azimuthally averaged temperatures.

adopted $h(R) = h_{100}^{\text{small-dust}} (R/100[\text{AU}])^\beta$, where $h_{100}^{\text{small-dust}}$ is the dust scale height at 100 AU radius. We determined the value of β using MCMC fittings.

Referencing to the previous studies (Dong et al. 2012; Hashimoto et al. 2015; Long et al. 2018; Keppler et al. 2019), we assumed the total dust mass in the small-dust disk to be $0.330 M_\oplus$; we assumed the dust composition to be 70% mass in silicate and 30% mass in graphite (Laor & Draine 1993); we assumed $a_{\min}^{\text{small-dust}}$ and $a_{\max}^{\text{small-dust}}$ to be $0.001 \mu\text{m}$ and $0.15 \mu\text{m}$, respectively. Since the main purpose for the optimization of the free parameters of the small-dust disk is to establish a realistic thermal profile, the exact dust mass, sizes and composition in the small-dust disk is not important as long as the optical and infrared SED can be reproduced in the synthetic observations.

Initially, we tried simultaneously determining the values of the four parameters, R_c , β , $h_{100}^{\text{small-dust}}$, and δ_{cav} using MCMC fittings. We found that there is a degeneracy between the values of R_c and δ_{cav} . Therefore, we re-ran the MCMC fitting with the value of δ_{cav} fixed to 0.001, to determine the values of the remaining three free parameters.

C.2.2. (Sub)millimeter rings

Motivated by the $\sim 2000 \mu\text{m}$ and $\sim 3000 \mu\text{m}$ intensity profiles resolved in the present study and in the previous works (Liu et al. 2024a; Doi et al. 2024), we parametrized the dust mass surface density distributions of grown dust grains (Figure C.2) in the following ways. We assumed that the (vertically integrated) dust mass column density profiles of the narrow- and wide-rings can be approximated by the Gaussian distributions for a certain range of radius (see below)

$$\Sigma^{\text{ring}}(R) = \Sigma_0^{\text{ring}} \exp \left[-\frac{(R - R_0^{\text{ring}})^2}{2(\sigma^{\text{ring}})^2} \right], \quad (\text{C.5})$$

where R_0^{ring} is the centroid radius of the dusty ring, Σ_0^{ring} is the dust mass column density at the radius $R = R_0^{\text{ring}}$ (i.e., the peak dust column density), and σ^{ring} is the characteristic width of the ring. We defined the inner and outer truncation radii $tr_{\text{in}}^{\text{ring}}$ and $tr_{\text{out}}^{\text{ring}}$ and let $\Sigma^{\text{ring}}(R > (R_0^{\text{ring}} + tr_{\text{out}}^{\text{ring}})) = 0$ and $\Sigma^{\text{ring}}(R < (R_0^{\text{ring}} - tr_{\text{in}}^{\text{ring}})) = 0$. Based on MCRT simulations, we found that the truncations are necessary. Otherwise, the extended rims of the rings will produce too strong far-infrared emission despite the fact that such diffused faint outer rims may not be detectable in the presented ALMA observations. Although the sharp truncation appears artificial, limited by angular resolution and sensitivities, its effects are hard to resolve with the present ALMA observations. In another phrase, the present observations do not well constrain exactly how column density profiles are truncated in the radial direction.

Based on fitting the radial intensity profiles of the ALMA Bands 3, 4, 6, and 7 images, we determined $R_0^{\text{narrow-ring}}$ to be 77.5 AU. For simplicity, we assumed $R_0^{\text{wide-ring}} = R_0^{\text{narrow-ring}}$. In the subsequent MCRT simulations, we verified that this assumption allows producing a model that looks similar to our observations.

The volume density distributions were evaluated based on an Equation that is analogous to Equation C.4. We adopted $h^{\text{narrow-ring}}(R) = h^{\text{wide-ring}}(R) = h_{100}^{\text{ring}} (R/100[\text{AU}])^{\beta^{\text{ring}}}$. The value of β^{ring} cannot be constrained by the present observations. Following the previous studies (Hashimoto et al. 2012; Dong et al. 2012), we assumed that the small-dust disk and the embedded grown dust structures have the same indices of scale height (i.e., $\beta^{\text{ring}} = \beta$). The previous study (Dong et al. 2012) found that the scale height of the embedded grown dust structures need to be ~ 10 times smaller than that of the small-dust disk, otherwise, the

synthetic far-infrared spectrum will appear over-luminous. We verified this by interactively varying $h_{100}^{\text{narrow-ring}}$ and $h_{100}^{\text{wide-ring}}$ in the MCRT simulations. We found that, as long as h_{100}^{ring} is smaller than $h_{100}/10$, the far-infrared spectrum becomes no more sensitive to h_{100}^{ring} . The scale heights can also affect the polarization properties at 873 μ m wavelength. At 873 μ m wavelength, the PDS 70 (sub)millimeter ring is only marginally optically thick in the vertical direction. Adopting a large scale height will make the ring less optically thick in the azimuthal direction, which makes the patterns of polarization position angles appear more like the case of a ring rather than that of an inclined disk (Kataoka et al. 2015; Yang et al. 2016, 2025), which is not consistent with the observations (Figure 1). On the other hand, adopting a very small scale height will lead to complicated patterns of polarization position angles at the inner and outer rims of the rings (Ohashi et al. 2020), which were not resolved in our observations. To avoid the over-luminous synthetic far-infrared spectrum and the (synthetic) pattern of polarization position angles that were not resolved in the ALMA observations, we chose $h_{100}^{\text{narrow-ring}} = h_{100}^{\text{wide-ring}} = 0.45$ AU. The detailed modeling for constraining scale height (Yang et al. 2025), which may be confused by the potential azimuthal variation of a_{max} in the specific case of PDS 70, is beyond the scope of the present paper.

We assumed the standard DSHARP (water-ice-coated) dust composition (Birnstiel et al. 2018) since both rings are situated outside the ~ 150 K water snowline (Figure C.2). We produced the opacity tables using the distribution of hollow spheres (DHS) approach and set the maximum volume fraction f_{max} to 0.8, which is the default of `optool`, to model deviations from perfect spherical symmetry and low-porosity aggregates. This approach is different from the DSHARP opacity tables released in Birnstiel et al. (2018) which assumed compact spherical grains. We checked and found that the differences between our opacity tables and the DSHARP opacity tables are very small. We assumed the minimum grain sizes $a_{\text{min}}^{\text{narrow-ring}} = a_{\text{min}}^{\text{wide-ring}} = 0.1$ μ m, while the evaluated dust opacities are not sensitive to the minimum grain sizes. Based on numerical simulations, Pinilla et al. (2024) argued that 0.1 μ m is the largest possible a_{min} that can maintain the inner disk of the PDS 70 system, although there may be model uncertainties. We tentatively assumed $a_{\text{max}}^{\text{narrow-ring}} = a_{\text{max}}^{\text{wide-ring}} = a_{\text{max}}^{\text{ring}}$, since the present high angular resolution ALMA Bands 3 and 4 observations lack the sensitivity to determine $a_{\text{max}}^{\text{narrow-ring}}$ and $a_{\text{max}}^{\text{wide-ring}}$ independently. Nevertheless, this assumption is very well motivated by the features of spectral indices and dust polarization described in Section 3.

The value of $tr_{\text{in}}^{\text{wide-ring}}$ was chosen such that $R_0^{\text{wide-ring}} - tr_{\text{in}}^{\text{wide-ring}} = R_{\text{gap}}$, which can make the synthesized infrared images and flux densities consistent with observations. The intensity distributions at infrared bands are less sensitive to $tr_{\text{out}}^{\text{wide-ring}}$. The observations at (sub)millimeter bands do not constrain $tr_{\text{out}}^{\text{wide-ring}}$ with high precision due to (1) the outer ring of the wide-ring is faint, and (2) the effect of convolving with the synthesized beam. Our present 873 μ m observations significantly detected the PDS 70 ring out to ~ 100 AU radius. After some trials with MCRT simulations, we chose $tr_{\text{out}}^{\text{wide-ring}} = 12$ AU, such that $R_0^{\text{ring}} + tr_{\text{out}}^{\text{wide-ring}} = 89.5$ AU. In such case, adding one FWHM of a $\sim 0''.1$ synthesized beam to $R_0^{\text{ring}} + tr_{\text{out}}^{\text{wide-ring}}$ will yield a ~ 100 AU detectable outermost radius. We found that this meet the impression of the observations presented in this paper and in the previously published radial intensity profiles (Doi et al. 2024). We note that limited by angular resolution, fundamentally, it is hard for our model to discern the errors in the length scales that are smaller than $\sim 0''.1/2.35 \sim 4.8$ AU (i.e., 1- σ beam width). We based on the MCRT simulations and the MCMC method to optimize the remaining free parameters, $a_{\text{max}}^{\text{ring}}$, $\Sigma_0^{\text{wide-ring}}$, $\sigma^{\text{wide-ring}}$, $\Sigma_0^{\text{narrow-ring}}$, $\sigma^{\text{narrow-ring}}$, $tr_{\text{in}}^{\text{narrow-ring}}$, and $tr_{\text{out}}^{\text{narrow-ring}}$.

C.2.3. Crescents

It is clear that reproducing the northwest crescent in the synthesized (sub)millimeter images requires including an azimuthally asymmetric dusty structure in our model. In addition, we found that it is not possible to reproduce a (sub)millimeter peak in the south that is offset from the projected major axis, unless we include yet another dusty crescent in the southwest. The geometry of dusty crescents remain poorly constrained by observations. Motivated by the previous modeling for the IRS 48 dusty crescent (van der Marel et al. 2013; Ohashi et al. 2020), we assumed the following two-dimensional dust mass column density profile for certain ranges of radius and deprojected position angle (see below)

$$\Sigma^{\text{crescent}}(R, \phi) = \Sigma_0^{\text{crescent}} \exp \left[-\frac{(R - R_0^{\text{crescent}})^{p_r}}{2(\sigma_{\text{crescent}})^{p_r}} \right] \exp \left[-\frac{(\phi - \phi_0^{\text{crescent}})^{p_{\phi}}}{2(\sigma_{\phi}^{\text{crescent}})^{p_{\phi}}} \right], \quad (\text{C.6})$$

where $\Sigma_0^{\text{crescent}}$ is the peak dust mass column density, R_0^{crescent} is the centroid radius, σ^{crescent} is the characteristic width in the radial direction, ϕ_0^{crescent} is the deprojected centroid position angle, ϕ_0^{crescent} is the characteristic width in the azimuthal direction (in degree unit), p_r is the index of radial density profile, and p_{ϕ} is the index of azimuthal density profile. We defined the inner and outer truncation radii $tr_{\text{in}}^{\text{crescent}}$ and $tr_{\text{out}}^{\text{crescent}}$ and let $\Sigma^{\text{crescent}}(R > (R_0^{\text{crescent}} + tr_{\text{out}}^{\text{crescent}})) = 0$ and $\Sigma^{\text{crescent}}(R < (R_0^{\text{crescent}} - tr_{\text{in}}^{\text{crescent}})) = 0$ such that the model does not appear over-luminous at infrared bands.

Motivated by the previous MCRT modeling for the IRS 48 dusty crescent (van der Marel et al. 2013; Ohashi et al. 2020), we assumed $p_r = 4$ for the northwest and southwest crescents. We found that the assumption of a high index of azimuthal density profile (e.g., $p_{\phi} = 4$) cannot reproduce the extended northwest crescent resolved in PDS 70 (Figure 1, 2). In the present work, We adopted $p_{\phi} = 2$. For both crescents, using MCRT modeling, we found that making R_0^{crescent} close to the centroid radius of the ring, 77.5 AU, can yield synthesized (sub)millimeter images that resemble the observed ones. Therefore, we fixed the R_0^{crescent} of both crescents to 77.5 AU.

We evaluated the volume density distributions based on an equation that is analogous to Equation C.4, assuming that the scale heights do not depend on the azimuth angle ϕ and is identical to the scale heights of the narrow- and wide-rings. The assumptions of dust opacities for the crescents are similar to those for the wide- and narrow-rings (Section C.2.2).

For each crescent, we based on the MCRT simulations and the MCMC method to optimize the remaining free parameters, $a_{\max}^{\text{crescent}}$, $\Sigma_0^{\text{crescent}}$, σ^{crescent} , $tr_{\text{in}}^{\text{crescent}}$, $tr_{\text{out}}^{\text{crescent}}$, ϕ_0 , and $\sigma_{\phi}^{\text{crescent}}$.

C.3. Radiative transfer

We performed MCRT modeling using the RADMC-3D code (Dullemond et al. 2012). To activate full treatment of dust polarization, we set `scattering_mode_max` = 5. We activated the modified random walk (of photons) by setting `modified_random_walk`=1. We note that the default of RADMC-3D is not activating the modified random walk, in case that it lead to less accurate results. Nevertheless, we have compared the MCRT simulations with and without activated the modified random walk and found no noticeable differences in the synthetic observations. Activating the modified random walk is beneficial for our MCMC fittings since it accelerates the simulations for systems with high optical depths, which is our present case. We adopted the RADMC-3D default for the maximum number of dust scattering, `mc_scat_maxtauabs`=30.

For each set of chosen free parameters, we first made a thermal run (i.e., using the `mctherm` command) to determine the dust temperatures (Figure C.2). In the thermal runs, the density files simultaneously incorporated the small-dust disk, wide-ring, narrow-ring, northwest crescent, and southwest crescent (Section C.2.1, C.2.2 C.2.3). We found that close to the host protostar where radiation field is strong, the derived temperatures of the small-dust disk can exceed the \sim 1500 K dust sublimation temperature (Pollack et al. 1994). To be realistic, after the thermal run, we edited the dust volume density by zeroing it in the regions with >1500 K temperature. Without making this edit, the synthesized optical and infrared SED cannot be consistent with the observed one. We produced the synthesized SEDs and images based on the temperature distributions derived from the thermal run and the edited dust volume density.

C.4. Caveats and limitations

The purpose of our MCRT model is to verify the plausibility of our current interpretation of the observations of PDS 70, rather than to precisely reproduce the intensity distributions. From the point of view of observational data, reproducing the (sub)millimeter intensity distributions resolved in the PDS 70 disk is subject to a few uncertainties.

Firstly, determining the inclination for an azimuthally asymmetric (sub)millimeter ring is challenging. Earlier studies (Hashimoto et al. 2012; Dong et al. 2012; Hashimoto et al. 2015; Long et al. 2018) suggested an inclination of 45° , while later works (Kepler et al. 2019; Sierra et al. 2025) proposed an inclination of 51.7° . Upon visually inspecting and fitting ellipses to the (sub)millimeter images (see Figure 2), we found that the inclination likely falls between 45° and 51.7° , at least for certain radius ranges. Our MCRT simulations indicate that assuming a constant inclination of 51.7° is a reasonable approximation, whereas a constant inclination of 45° is inconsistent with the (sub)millimeter interferometric observations. Although one should bear in mind that a constant inclination in the model is merely an approximation, nevertheless, the range of probable inclinations, either uniform or dependent on radius and azimuthal angle, is small. We found that changing inclination from 51.7° to 45° does not yield noticeable changes in the synthesized optical and infrared spectrum. Although the small error in the inclination may lead to discrepancies between the synthesized and observed (sub)millimeter intensity distributions, it is unlikely to dramatically change our overall interpretation for the dust sizes and dust mass column densities (Liu et al. 2022).

Second, the observations of the polarization fraction at $873\text{ }\mu\text{m}$ wavelength and the total intensities at 2068 and $3075\text{ }\mu\text{m}$ wavelengths are still subject to limited SNR. This limitation hampers our ability to diagnose the detailed morphologies of the dusty crescents and the spatial dependence of a_{\max} . For example, it is still challenging for us to diagnose the a_{\max} in the narrow-ring and wide-ring separately. Instead, we had to assume that their a_{\max} values are comparable. Moreover, besides the two crescents, there might be more embedded localized dust concentrations which cannot be resolved due to the limited angular resolution and sensitivities of our present ALMA Bands 3 and 4 observations, and due to the high optical depths at shorter wavelength bands (Liu et al. 2024b). This possibility cannot be considered in our radiative transfer modeling, which may lead to discrepancies between the synthesized and observed (sub)millimeter intensity distributions. This can also confuse the pixel-by-pixel fittings to the (sub)millimeter SEDs. It is possible to diagnose the embedded dusty concentrations using a multi-components approach in the SED fittings (Li et al. 2017; Liu et al. 2019, 2024b,a), although it remains difficult to carry out such analyses systematically. Finally, the infrared spectra of PDS 70 presented time variabilities (Long et al. 2018; Liu et al. 2025), which led to uncertainties in the derived thermal profiles.

In terms of model, our present approach also involved simplifications. This is partly due to our compromise to limit computational costs, and partly due to the limited understanding of the system. For example, we assumed the azimuthally symmetric, power-law profiles for the scale heights of the rings and the crescents, instead of iteratively solving local scale heights based on MCRT simulations. The latter approach is not practical due to the prohibitive cost of computing power. Also, in reality, it is not hard to imagine that the scale height may have dependences on the azimuth angle due to planet-disk interaction. One should be cautious when applying the scale heights derived in our MCMC fittings to other studies. In MCRT simulations, errors in the scale heights will lead to errors in the derived thermal profiles, which, in turns, lead to errors in the synthesized intensity distributions. Given that the temperature distributions in our MCRT models are relatively smooth (Figure C.2), we do not consider this effect significant, in particular, in the Rayleigh-Jeans limit (e.g., frequency bands of the presented ALMA observations).

Our present assumptions of the crescent geometry are not necessarily realistic. In addition, it is not necessarily realistic to assume a constant a_{\max} value within a crescent (Cazzoletti et al. 2018). The assumption of position-angle-independent crescent width σ^{crescent} (Section C.2.3) may also be regarded as a simplification. The comparison between our model and the observations indicated that a considerable fraction of the dust in the crescents has $a_{\max} \lesssim 100\text{ }\mu\text{m}$. It does not rule out the previous claim that some millimeter-sized dust is embedded in the crescents or other unresolved localized substructures (Liu et al. 2024a).

Table C.1: Parameters of the fiducial model derived from MCMC fittings

Small-dust disk						
R_c (AU)	β	h_{100} (AU)				
$55.0^{+1.9}_{-2.0}$	$1.254^{+0.008}_{-0.010}$	$9.14^{+0.19}_{-0.19}$				
Narrow-ring and wide-ring						
a_{\max}^{ring} (μ m)	$\Sigma_0^{\text{wide-ring}}$ (g cm^{-2})	$\sigma^{\text{wide-ring}}$ (AU)	$\Sigma_0^{\text{narrow-ring}}$ (g cm^{-2})	$\sigma^{\text{narrow-ring}}$ (AU)	$tr_{\text{in}}^{\text{narrow-ring}}$ (AU)	$tr_{\text{out}}^{\text{narrow-ring}}$ (AU)
87^{+10}_{-9}	$0.093^{+0.007}_{-0.015}$	18^{+3}_{-1}	$0.4^{+0.35}_{-0.01}$	$3.2^{+0.1}_{-0.4}$	$4.9^{+0.8}_{-0.6}$	15^{+1}_{-1}
Northwest crescent and southwest crescent						
$a_{\max}^{\text{crescent-NW}}$ (μ m)	$\Sigma_0^{\text{crescent-NW}}$ (g cm^{-2})	$\sigma^{\text{crescent-NW}}$ (AU)	$tr_{\text{in}}^{\text{crescent-NW}}$ (AU)	$tr_{\text{out}}^{\text{crescent-NW}}$ (AU)	$\phi_0^{\text{crescent-NW}}$ ($^{\circ}$)	$\sigma_{\phi}^{\text{crescent-NW}}$ ($^{\circ}$)
79^{+44}_{-24}	11^{+1}_{-1}	$4.0^{+0.5}_{-0.4}$	$3.9^{+0.6}_{-1.0}$	$6.4^{+0.2}_{-0.1}$	317^{+1}_{-1}	$15.7^{+0.3}_{-0.2}$
$a_{\max}^{\text{crescent-SW}}$ (μ m)	$\Sigma_0^{\text{crescent-SW}}$ (g cm^{-2})	$\sigma^{\text{crescent-SW}}$ (AU)	$tr_{\text{in}}^{\text{crescent-SW}}$ (AU)	$tr_{\text{out}}^{\text{crescent-SW}}$ (AU)	$\phi_0^{\text{crescent-SW}}$ ($^{\circ}$)	$\sigma_{\phi}^{\text{crescent-SW}}$ ($^{\circ}$)
38^{+11}_{-11}	$0.15^{+0.01}_{-0.01}$	11^{+1}_{-1}	$7.2^{+1.0}_{-1.3}$	$7.8^{+0.3}_{-0.5}$	225^{+3}_{-3}	$12.7^{+1.5}_{-1.4}$

Presently, we do not consider the segregation of dust sizes and compositions in the vertical direction. We think our present approach provides good estimates for the properties of the dust that dominates the continuum luminosity at ~ 870 – 3000 μ m wavelengths. However, there might be a layer of disk atmosphere that the a_{\max} value (e.g., ~ 10 μ m) is in between those of the small-dust disk and the rings and crescents (Sierra et al. 2025). Failing to consider this layer of disk atmosphere may lead to significant errors in the intensity distributions at wavelengths $\lesssim 500$ μ m (Sierra et al. 2025). The errors in our synthesized 160 μ m flux density (Section ??) may also be partly or largely attributed to this issue. On the other hand, constraining the properties of this layer of disk atmosphere requires multi-wavelength observations at $\lesssim 500$ μ m wavelengths, which is not available presently. In this work, we relied on MCRT simulations to derive temperature distributions. We avoided deriving temperature distributions based on fitting ~ 400 μ m wavelength observations (e.g., ALMA Band 9 observations), to bypass the systematics caused by the limited understanding of the disk atmosphere. Nevertheless, our derived temperature distributions for grown ($\gg 1$ μ m) dust appear reasonable as compared to those derived in the SED fittings that included Band 9 observations (Sierra et al. 2025). The disk atmosphere has a small amount of dust mass and should be very optically thin at > 870 μ m wavelength, which does not significantly affect the scientific discussion of our present work.

We do not try to model the inner disk in detail. This is because the inner disk was insufficiently spatially resolved in multi-wavelength observations, and may be confused by non-dust emission mechanisms (Liu et al. 2024a). The models for the inner disk will naturally be very degenerated, therefore lack predicting power. The attempts to model it will include many more free parameters, making the MCMC fittings less easy to converge. In addition, it makes it more difficult to diagnose the posteriors of the free parameters since the parameter space will have higher dimensions.

Finally, the uncertainties in dust opacities and dust compositions remain fundamental to all studies that involved fitting (sub)millimeter SEDs, which have been elaborated in some recent studies (Yang & Li 2020; Chung et al. 2024; Guidi et al. 2022). We note that while we adopted the default DSHARP dust opacities presented in Birnstiel et al. (2018), based on a population synthesis study, Delussu et al. (2024) suggested that a modified opacity table may be more realistic than the original DSHARP opacities. However, the population synthesis of Delussu et al. (2024) yielded too low dust spectral indices at 1–3 mm wavelengths to be consistent with the recent surveys of protoplanetary disks (Chung et al. 2025; Painter et al. 2025). Therefore, we do not adopt the updates recommended in Delussu et al. (2024). In addition, given the potential segregation of dust sizes and dust compositions, the compositions of small dust constrained by analyzing infrared spectra are not necessarily representative of the compositions of grown dust that resides in the disk mid-plane. Moreover, while some observational studies have considered a weakly-porous dust morphology (Stephens et al. 2023), we note that evaluating the opacities for porous dust grains remain theoretically challenging and computationally costly (Kataoka et al. 2014; Tazaki & Tanaka 2018). The publicly available codes may not necessarily provide accurate estimates for the opacities of porous dust in the regime of $a_{\max} \gtrsim \lambda/2\pi$. Given that the recent studies favour low porosities (Tazaki et al. 2019; Stephens et al. 2023), we tentatively assumed a compact dust morphology for simplicity. This may lead to underestimates of a_{\max} by up to a few times although it is not necessary the case.

Given the good fidelity achieved by our ALMA images (Figure 1, 2), we consider the effects mentioned above more important than the effects of the potential interferometric imaging artifacts, which are not trivial to quantitatively assess in an azimuthally asymmetric system. In fact, thermal noises in the ALMA Bands 3 and 4 images are likely more important than the interferometric imaging artifacts. Our present approach of performing modeling in the image instead of the visibility domain benefits from a lower numerical cost, since we do not need to perform Fourier transformation for the MCRT model, and since we can break down the modeling framework into the fittings for a few spatially isolated features.

Instead, the actual dust column density may increase more steeply toward the centroid radius of the narrow-ring than the Gaussian profile.

Appendix D: Dust fragmentation velocity

We derived the fragmentation velocity v_{frag} based on the following equation (Birnstiel et al. 2016)

$$a_{\max} \simeq \frac{\Sigma_g}{\rho_s \alpha_{\text{vis}}} \left(\frac{v_{\text{frag}}}{c_s} \right)^2, \quad (\text{D.1})$$

where α_{vis} is a dimensionless parameter that characterizes turbulence and viscosity in a viscous accretion disk, $c_s = \sqrt{\frac{k_B T}{\mu m_H}}$ is the thermal sound speed, $\mu = 2.33$ is the mean molecular weight, and $m_H = 1.67 \times 10^{-24}$ g is the mass of a hydrogen atom. We assumed the material density of dust grains $\rho_s = 3 \text{ g cm}^{-3}$ (Birnstiel et al. 2016), and tentatively assumed $\alpha_{\text{vis}} = 10^{-3}$ (Sierra et al. 2025); we adopted the temperature T determined from our radiative transfer simulation. We derived Σ_g based on the overall dust density in our model, assuming a gas-to-dust mass (g) ratio of 100 (Yoshida et al. 2025).

Since we do not consider dust porosity, the assumed value of ρ_s may be overestimated by up to 1 order of magnitude (Tazaki et al. 2019; Stephens et al. 2023), while we might underestimate a_{\max} by a few times. These effects of overestimating ρ_s and underestimating a_{\max} compensate for each other in the derivation of v_{frag} . Therefore, we do not think the assumption of a compact instead of slightly (e.g., $\sim 90\%$) porous grain morphology will significantly bias the derivation of v_{frag} .

Assuming $g = 100$ may overestimate Σ_g , since the gas-to-dust mass ratio may be lowered in dust traps (Birnstiel et al. 2016). This leads to underestimates of v_{frag} . This may be more concerning for the dust narrow-ring and the dust crescents, as these structures could represent dust traps that have lower g values (Figure 4). Conversely, if a significant fraction of dust mass is removed from the wide-ring due to dust migration, the assumption of $g = 100$ may underestimate Σ_g in the wide-ring, leading to overestimates of v_{frag} . For this reason, we avoided discussing v_{frag} inside the (sub)millimeter cavity as it would be significantly overestimated.

Planet-disk interaction may induce turbulence (Bi et al. 2021; Dong et al. 2019), which effectively enhances the value of α_{vis} . Without considering this mechanism may lead to underestimates of α_{vis} , thereby underestimating v_{frag} . Nevertheless, our presently assumed α_{vis} value is already relatively high. It is not very likely that our assumed α_{vis} value is significantly underestimated.